PHYSICAL REVIEW B **110**, 035150 (2024)

Optimal half-metal band structure for large thermoelectric performance

Finantius E. M. Rahangiar,[1,2] Adam B. Cahaya,[3] Melania S. Muntini,[4] Isa Anshori,[5,6] and Eddwi H. Hasdeo[2,7]
[1]*Department of Physics, Universitas Gadjah Mada, Sekip Utara BLS 21, Yogyakarta 55281, Indonesia*
[2]*Research Center for Quantum Physics, National Research and Innovation Agency, South Tangerang 15314, Indonesia*
[3]*Department of Physics, Faculty of Mathematics and Natural Sciences, University of Indonesia, Depok 16424, Indonesia*
[4]*Department of Physics, Faculty of Science and Data Analytics, Institut Teknologi Sepuluh Nopember, Surabaya 60111, Indonesia*
[5]*School of Electrical Engineering and Informatics, Bandung Institute of Technology, Bandung 40132, West Java, Indonesia*
[6]*Research Center for Nanosciences and Nanotechnology, Bandung Institute of Technology, Bandung 40132, West Java, Indonesia*
[7]*Department of Physics and Material Science, University of Luxembourg, L-1511 Luxembourg, Luxembourg*

(Received 8 January 2024; revised 3 July 2024; accepted 8 July 2024; published 22 July 2024)

Half-metal ferromagnets were predicted [Cahaya, Tretiakov, and Bauer, IEEE Trans. Magn. **51**, 1 (2015)] to give large thermoelectric performance in antiparallel spin valve configuration. Despite being metals that suffer from the Wiedemann-Franz law, the additional spin degrees of freedom allow for tuning of the thermoelectric properties due to the spin valve enhancement factor. We test this theory and find a mismatch of parameters that gives large thermoelectric performance and large spin valve enhancement factor. As a result, we show that the spin valve setup is useful only for half-metal ferromagnets with initially poor thermoelectric performance. To obtain the largest thermoelectric performance, one still needs to open the band gap.

DOI: 10.1103/PhysRevB.110.035150

I. INTRODUCTION

Thermoelectric (TE) materials are capable of transforming heat into electricity. Despite the fact that research on this topic has been conducted for centuries, it is still difficult to obtain TE materials for practical applications. The power factor PF $= S^2\sigma$ and the dimensionless figure of merit $ZT = (\mathrm{PF}/\kappa)T$ are two parameters used to determine whether a material is suitable for TE purposes. Here, S is the Seebeck coefficient, σ is the electrical conductivity, κ is the thermal conductivity, and T is the average of the hot and cold temperatures. Much effort has been put into improving both ZT and PF. Thermoelectric performance can be increased by either increasing PF or reducing thermal transport. Common methods for this include using low-dimensional structures [1–4] and manipulating the band structure [5] through doping [6] and strain [7,8]. Recent progress in topological insulators enables a dissipationless edge channel to enhance thermoelectric performance [9,10]. The other method is by enhancing phonon scattering [11] to reduce phonon transport [12,13].

Metals are not ideal TE materials because electrons that carry charge current also carry heat, which obeys the Wiedemann-Franz law $\sigma T/\kappa = (3k_B^2)/(\pi^2 e^2)$, where k_B is the Boltzmann constant and e is the charge of an electron [14]. In addition, the Seebeck coefficient, which is the ratio of electric field to temperature gradient ($S = -\nabla V/\nabla T$), is very small in metals, resulting in a ZT value that is much less than 1. Despite the small TE efficiency of metals, the power factor can be large. Currently, $\mathrm{Mg_3Bi_2}$-based materials possess one of the largest PF about 20 $\mu\mathrm{W/cm\,K^2}$ [15]. This large PF is useful when there is an unlimited heat source and output power is prioritized over efficiency.

When spin degrees of freedom are involved in TE transport [16], both the PF and ZT of metals can be further increased [17]. In Fig. 1(a), half-metal ferromagnets (HMFs) with opposite spin majority in two legs are connected by a normal metal. The Seebeck coefficients in both legs are assumed to be of equal and opposite sign (S and $-S$). In this antiparallel setup, the spin accumulation at the spacer is maximized due to low spin transfer from one leg to the other. As a result, the voltage and temperature gradients across the thermocouple are maximized [18] and consequently so are ZT and PF [17,19]. This effect is referred to as the spin valve enhancement factor (SVEF).

A previous work considered half-metallic two-dimensional (2D) chromium pnictides [19]. They predict the enhancement of ZT for CrAs, CrSb, and CrBi but not in CrP. In some values of the Fermi energy, the SVEF is less than unity, indicating that no enhancement has been achieved. Therefore, it is necessary to find the optimal band structure and parameters to achieve the largest PF and ZT in this system. In this paper, we start with the simplest model of the half-metal band structure and find the optimal parameters to obtain the largest SVEF, PF, and ZT. We describe a half metal as spin-polarized bands comprising a single metallic band [blue line in Fig. 1(b)] and two insulating bands [red lines in Fig. 1(b)] with a band gap 2Δ and opposite spin orientation. We model the metallic band as a single parabolic band that has a finite density at equilibrium determined by its band depth E_0 measured from the charge neutrality point $\mu = 0$. Since we consider 2D materials, the Fermi energy μ is tunable by a gate voltage.

In this paper, we focus on optimizing TE quantities from electronic contributions and neglect the phonon contribution to thermal conductivity, κ_{ph}. Depending on materials, κ_{ph} will reduce ZT by small or large percentage. There exists, HMF with low thermal conductivity such as CrBi with $\kappa_{\mathrm{ph}} \approx 0.06$ W/mK compared with electronic thermal conductivity $\approx 10^2$ W/mK [19].

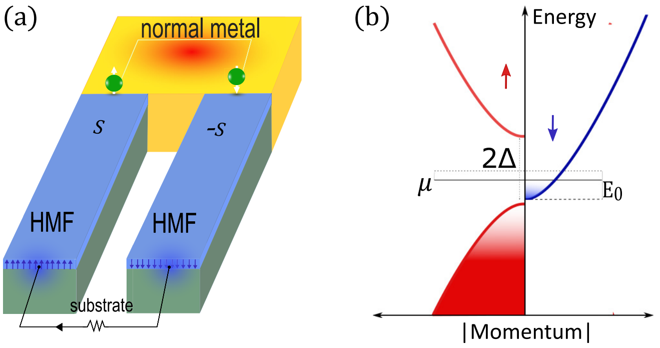

FIG. 1. (a) Spin valve configuration of the half-metal ferromagnetic insulator and (b) band structure of the half-metal ferromagnetic insulator using the parabolic band model.

II. MODEL AND METHODS

Here, we model a HMF system using a parabolic band for the spin-down metal state and two parabolic bands for the spin-up insulating state. The electronic band structures for metal is given by

$$E_m(\mathbf{k}) = \frac{\hbar^2\mathbf{k}^2}{2\bar{m}} - E_0, \tag{1}$$

while for insulator E_i it consists of

$$E_c(\mathbf{k}) = \frac{\hbar^2\mathbf{k}^2}{2\bar{m}} + \Delta, \tag{2}$$

$$E_v(\mathbf{k}) = -\frac{\hbar^2\mathbf{k}^2}{2\bar{m}} - \Delta, \tag{3}$$

where E_0 is the depth of the metallic band and Δ is half of the band gap of insulating bands, as illustrated in Fig. 1(b).

We can vary the effective mass $\bar{m}$ for three bands; however, the TE kernel

$$\mathcal{L}_j^{(n)} = \sum_{N_j}\int \tau v_j^2(E)\mathcal{D}_j(E)(E-\mu)^n\left(-\frac{\partial f}{\partial E}\right)dE \tag{4}$$

defined in the linearization of the Boltzmann equation is independent of mass due to the cancellation of $\bar{m}$ in v^2 and $\mathcal{D}$ (see Appendix A). Here $j = m, i$ are indices for the metal and insulator band respectively with number of bands $N_m = 1$ and $N_i = 2$ which consist of $\{c, v\}$ bands. $\mathcal{D}_j(E) = \sum_{\mathbf{k}} \delta(E_j(\mathbf{k}) - E)$ is the density of states, τ is the relaxation time, and $v_j = \hbar^{-1}\partial E_j/\partial k_x$ is the longitudinal velocity of the electron. TE properties of our system are obtained using the Boltzmann transport equation with relaxation time approximation. We argue that a constant relaxation time independent of energy E is a good approximation in the 2D parabolic band due to the constant density of states. Later in Sec. IV B, we also estimate corrections due to an energy-dependent relaxation time $\tau(E)$. For simplicity, here we assume negligible phonon contribution to κ as shown in previous work [19].

Thermoelectric transport coefficients are given by

$$\sigma_j = e^2\mathcal{L}_j^{(0)}, \quad j = m, i, \tag{5}$$

$$S_j = -\frac{1}{eT}\frac{\mathcal{L}_j^{(1)}}{\mathcal{L}_j^{(0)}}, \tag{6}$$

$$\kappa_j = \frac{1}{T}\left(\mathcal{L}_j^{(2)} - \frac{\left(\mathcal{L}_j^{(1)}\right)^2}{\mathcal{L}_j^{(0)}}\right), \tag{7}$$

where σ, S, and κ are electrical conductivity, Seebeck coefficient, and electronic thermal conductivity. The transport coefficient of the whole system is described by [17]

$$\sigma_t = \sigma_i + \sigma_m, \tag{8}$$

$$S_t = \frac{\sigma_i S_i + \sigma_m S_m}{\sigma_i + \sigma_m}, \tag{9}$$

$$\kappa_t = \kappa_i + \kappa_m. \tag{10}$$

Using the transport coefficient of the system, we can define the figure of merit and power factor as well as their corresponding spin valve enhanced values as follows:

$$ZT_{\mathrm{v}} = \chi ZT = \chi\frac{\sigma_t S_t^2}{\kappa_t}, \tag{11}$$

$$\mathrm{PF}_{\mathrm{v}} = \chi\mathrm{PF} = \chi\sigma_t S_t^2, \tag{12}$$

where χ is the SVEF due to nonparallel configuration shown in Fig. 1(a) [17]. SVEF is given by

$$\chi = \frac{(1 - PP')^2}{1 - P^2}, \tag{13}$$

where P and P' are respectively related to spin polarization of charge and heat:

$$P = \frac{\sigma_m - \sigma_i}{\sigma_m + \sigma_i}, \tag{14}$$

$$P' = \frac{\sigma_m S_m - \sigma_i S_i}{\sigma_m S_m + \sigma_i S_i}. \tag{15}$$

Parenthetically, we neglect the spin-orbit coupling so that the polarizations can be given simply by Eqs. (14) and (15). In the presence of spin-orbit coupling, Eqs. (8)–(10) remain intact while for Eqs. (14) and (15) they should be defined through the spin projection procedure.

III. RESULTS

A. Thermoelectric coefficients

In Fig. 2, we show separately the thermoelectric coefficients (σ, S, and κ) of the spin-down state (metal) and spin-up state (insulator) and the total contribution of both spins as a function of the Fermi energy μ. We fix the band gap and vary the depth of the metallic band E_0. TE coefficients are plotted in units of $\sigma_0 = \tau_0 k_B T e^2/\pi L\hbar^2$, $S_0 = k_B/e$, and $\kappa_0 = \tau_0 k_B^3 T^2/\pi L\hbar^2$ where τ_0 is the relaxation time and L is confinement length. Using a typical confinement length $L = 1$ nm, $T = 300$ K, and $\tau_0 = 1$ fs, we obtain $\sigma_0 = 3043.1$ S/m, $S_0 = 86.1$ μV/K, and $\kappa_0 = 677.7$ μW/cm K.

As summations of contributions from the insulating and metallic bands, the electric σ_t and thermal κ_t conductivities of the half-metallic band possess values higher than those of each individual spin. Meanwhile, the Seebeck coefficient of the half-metallic band shows an insulating—or metallic—like character depending on the value of E_0 vs Δ. For E_0 larger than Δ, the Seebeck coefficient of half metal is monotonic and therefore has a similar character to metal. On the other

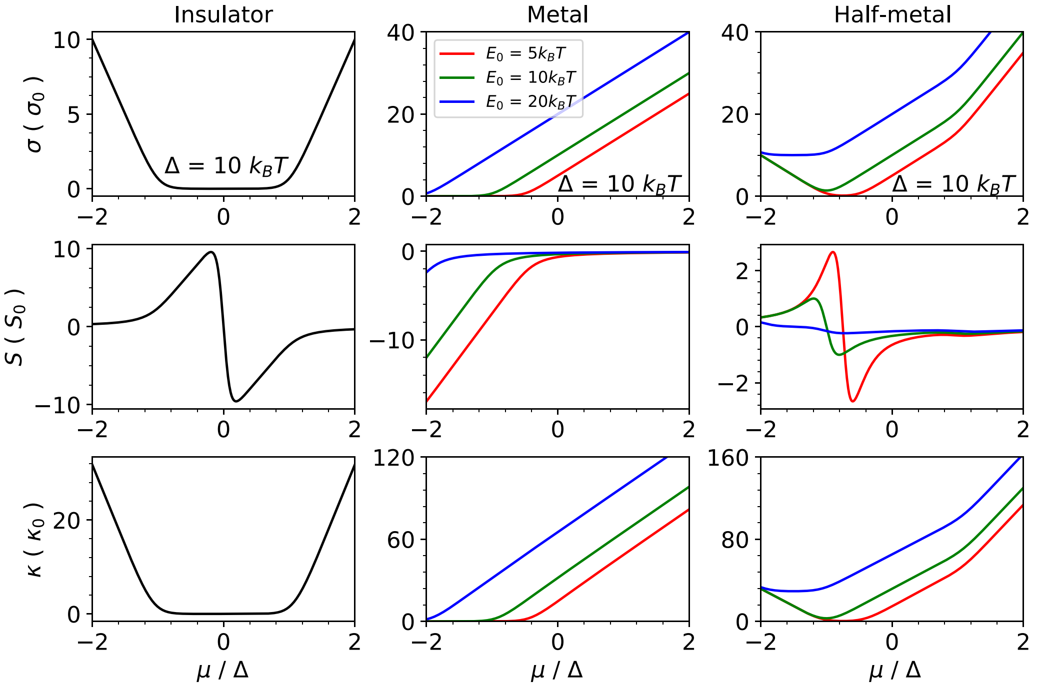

FIG. 2. Thermoelectric coefficients of insulator, metal, and half metal. Electrical conductivity, Seebeck coefficient, and thermal conductivity as a function of Δ and varying E_0.

hand, for E_0 smaller than Δ, the Seebeck coefficient shows an insulating-like character with the peak positions being shifted from the charge neutrality point $\mu = 0$. However, the combined Seebeck coefficient values on the HMF are lower than those of individual bands given by Eq. (9).

B. *ZT* and PF of half metals

Based on the results in Fig. 2, one can calculate dimensionless ZT and PF using Eqs. (8)–(10). In Fig. 3(a) we show the 2D plot of ZT as a function of μ and Δ for $E_0 = 2k_BT$. In the negative μ, we obtain a very large ZT above 2 (extended color bar). Taking a vertical cut of ZT along $\Delta = 6k_BT$, one observes double peak structures of ZT as a function of μ. These double peaks originate from S_t^2 (Fig. 2). Focusing on $\mu = \pm\Delta$ [Figs. 3(b) and 3(c)], we scan ZT over the $\Delta - E_0$ space. At $\mu = \Delta$, ZT is generally less than 1. On the other hand, at $\mu = -\Delta$, ZT can be higher than 2 as long as E_0 is smaller than Δ [see Fig. 3(c)]. This means that the ideal band structure to achieve the highest ZT is slightly gapped out with a band gap of approximately $\approx 3k_BT$ [see Fig. 3(d)]. We note that the region with large ZT extends to large values of E_0 and Δ. However, for large Δ one needs large doping via a gate voltage to reach $\mu = -\Delta$. We note, parenthetically, the value of μ can be smaller than $-\Delta$ as long as $E_0 > \Delta$. We have checked numerically that for $E_0 = c\Delta$ the values of PF, ZT, and SVEF are the same for $\mu = -\Delta$ and $-c\Delta$ (see Fig. 11 and Appendix C).

Next, we turn our attention to PF. The HMF power factor reaches a very high value at $\mu = \Delta$ and for very low Δ [see Fig. 4(a)]. Focusing on $\mu = \Delta$, we can obtain optimal Δ and E_0 in Fig. 4(b). Small $\Delta \approx 2$–$3k_BT$ and small $E_0 < 3k_BT$ produce very large $\text{PF} \approx 6\text{PF}_0$ where $\text{PF}_0 = 0.23 \times \bar{\tau}\ \mu\text{W/cm K}^2$, with $\bar{\tau}$ the relaxation time in femtoseconds. To reach the current record of PF, one requires a relaxation time of about 10 fs, which is a moderately clean sample. Some experiments and computational results of electron relaxation time have shown a higher value than 10 fs as in graphene around 300 fs [20–22]. For $\mu = -\Delta$, one can obtain a moderately large PF in the region where ZT is large [see Fig. 4(c)]. The optimal band structure for the largest PF is summarized

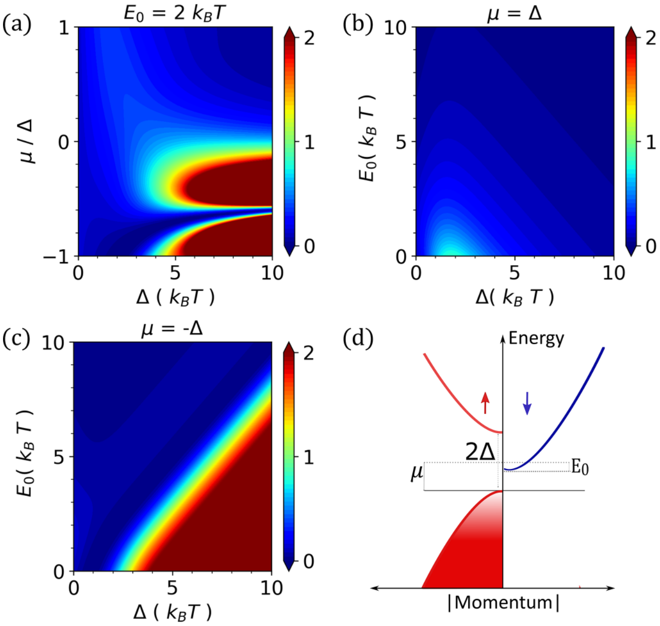

FIG. 3. (a) The 2D plot of ZT as a function of Fermi energy μ and Δ for $E_0 = 2k_BT$. (b), (c) ZT for $\mu = \Delta$ and $\mu = -\Delta$, respectively, plotted as a function of E_0 and Δ. (d) Optimal band structure to achieve optimal ZT.

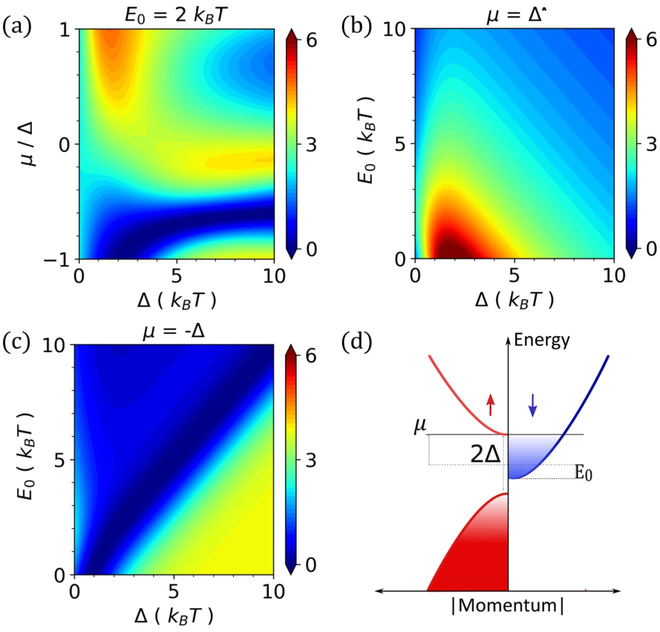

FIG. 4. (a) The 2D plot of PF as a function of μ and Δ for $E_0 = 2k_BT$. (b), (c) PF for $\mu = \Delta$ and $-\Delta$, respectively, plotted as a function of E_0 and Δ. (d) Optimal band structure to achieve the largest PF.

in Fig. 4(d). In this case, $\mu = \Delta$ and E_0 and Δ are very small, which means that we need to open the global HMF band gap about $\Delta - E_0$.

C. Spin valve enhancement factor

In Eqs. (11) and (12), thermoelectric performance is enhanced when SVEF > 1. Therefore, SVEF is expected to improve the TE performance of half metals. Figure 5(a) shows the SVEF of HMF as a function of the Fermi energy μ from $-\Delta$ to Δ. The solid lines are for $\Delta = 5k_BT$ and the dashed lines are for $\Delta = 20k_BT$, with each color representing different metallicity (E_0). The results show that a large band gap yields small values of SVEF at low Fermi energy and drastically increases near the band edge. SVEF increases greatly with the increase of E_0. In the limit of $E_0 \gg \Delta$, charge polarization is dominated by the metal sector which gives $P \approx 1$ [see Eq. (14)] in the entire range μ between $[-\Delta, \Delta]$. On the other hand, the values of P' can deviate from unity due to the large contribution of S_i near the band edges. The degrees of polarization P and P' are proportional to E_0/Δ. For small Δ, thermal carriers are excited above the gap giving the smeared profile of SVEF inside the gap (solid lines). The bigger E_0, the closer P value to unity at the edges, resulting in a linear increase in SVEF. The highest SVEF is achieved at $\mu = -\Delta$ because in these parameters S_i and S_m give opposite signs [see Eq. (15)] with $P' = 3$ and $P \approx 1$ for $E_0 \gg \Delta$. For $E_0 = 100k_BT$, SVEF reaches 100 at $\mu = -\Delta$ and about 20 at $\mu = \Delta$. Figure 5(b) illustrates the optimal band structure for the largest SVEF.

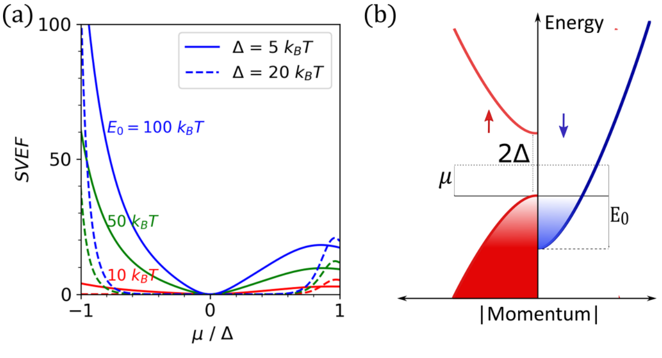

FIG. 5. (a) SVEF as a function of Fermi energy (μ/Δ) for various values of E_0. The dashed lines are for $\Delta = 20k_BT$ and the solid lines are for $\Delta = 5k_BT$. (b) Optimal band structure for large SVEF.

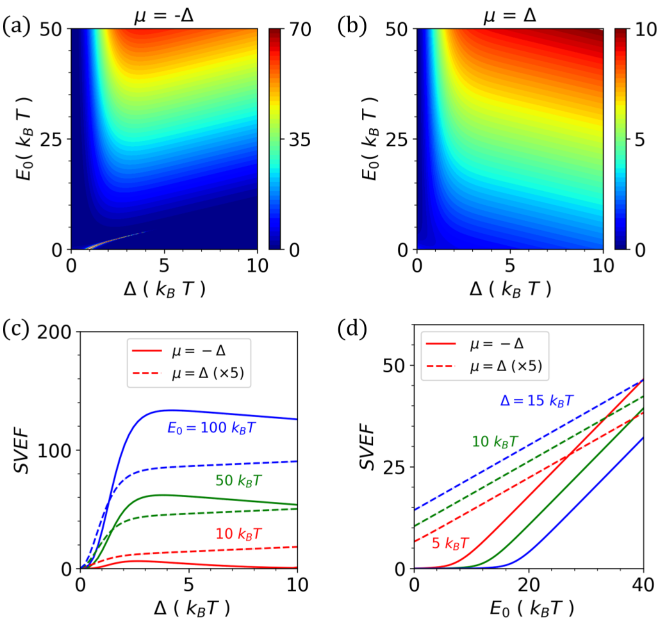

FIG. 6. SVEF of HMF in contour plots at two different Fermi energies (a) $\mu = -\Delta$ and (b) $\mu = \Delta$ as a function of E_0 and Δ. (c) SVEF as a function of Δ for several values of E_0. (d) SVEF as a function of E_0 for several values of Δ. In (c) and (d), the solid lines are for $\mu = -\Delta$ and the dashed lines are for $\mu = \Delta$. (The dashed lines are multiplied by 5 so that they can be plotted on the same scale.)

We focus on two values of $\mu = \pm\Delta$ and find the optimal E_0 and Δ for the best SVEF of the two cases. In Figs. 6(a) and 6(b), we show the 2D plot of SVEF as a function of E_0 and Δ for position μ, respectively, at $\mu = -\Delta$ and Δ. We take a horizontal cut of Figs. 6(a) and 6(b) and plot SVEF vs Δ in Fig. 6(c) for several values of E_0. For $\mu = -\Delta$ (solid lines), SVEF shows a peak with an optimal band gap Δ between 2 and $3k_BT$. Meanwhile, for $\mu = \Delta$ (dashed lines), the SVEF increases monotonically as a function of Δ. Taking a vertical cut of Figs. 6(a) and 6(b), we show that SVEF increases monotonically as a function of E_0 at both positions of μ [see Fig. 6(d)]. However, at $\mu = \Delta$ ($\mu = -\Delta$), the SVEF is proportional (inversely proportional) to Δ. In Figs. 6(c) and 6(d), we deliberately multiply SVEF values by 5 for the case of $\mu = \Delta$ to make comparisons with $\mu = -\Delta$.

As presented in Figs. 3 and 4, high TE performances require a very small value of E_0. On the other hand, as shown in Figs. 5 and 6, SVEF prefers large E_0. These different

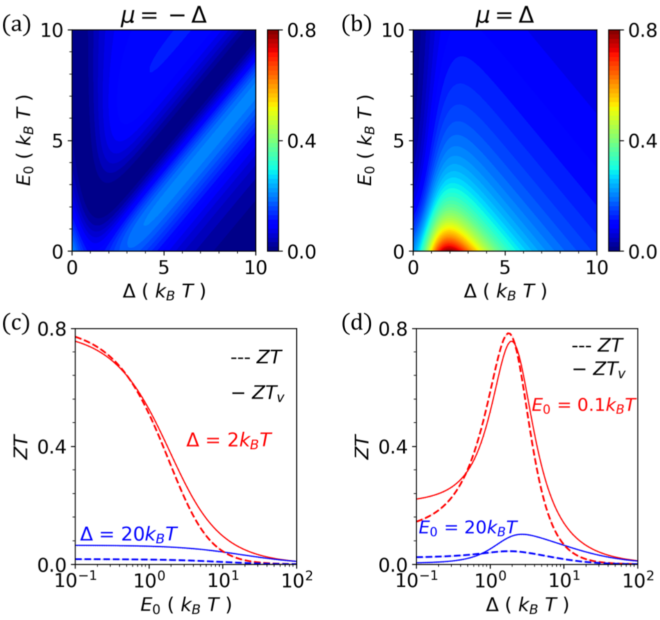

FIG. 7. (a), (b) 2D plots of ZT on the spin valve at $\mu = -\Delta$ and Δ, respectively, as a function of Δ and E_0. (c), (d) ZT as a function of E_0 and Δ, respectively, at $\mu = \Delta$.

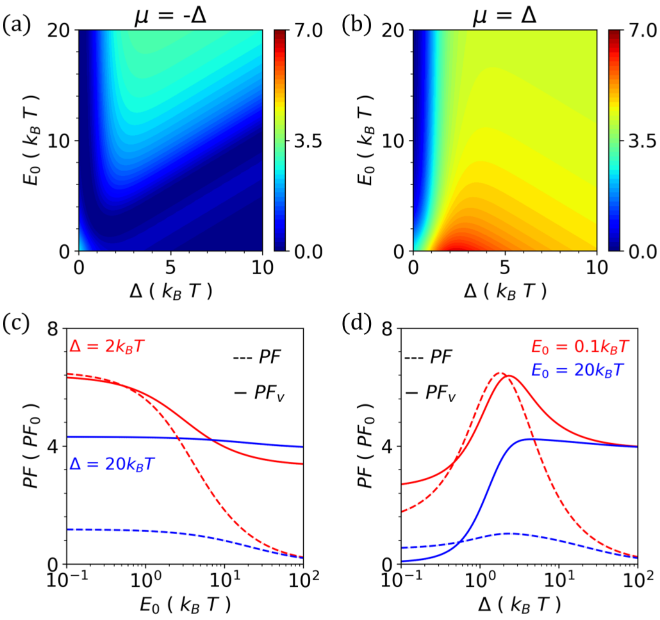

FIG. 8. (a), (b) 2D plot of PF on the spin valve at $\mu = -\Delta$ and Δ, respectively, as a function of Δ and E_0. (c), (d) Power factor as a function of E_0 and Δ, respectively, at $\mu = \Delta$.

conditions indicate the mismatch of parameters to obtain maximum SVEF with the parameters that contribute to large ZT and PF. For that reason, we cannot get both of them at the same time. Two-dimensional ferromagnetic insulators, for example CrI_3, which have a large band gap around 1.89 eV ($ZT = 1.57$ at $T = 900$ K) [23] thus do not have large SVEF and PF. Here, we calculate the ferromagnetic insulator by the four-band model, and it gives consistent results where SVEF is low (see Appendix B). ZT can be potentially large, but phonon thermal conductivity might hamper it. On the other hand, chromium pnictide such as CrBi is an HMF and has large Δ and E_0. This material has a large SVEF but the initial ZT is small [19].

IV. TE PERFORMANCE OF THE SPIN VALVE THERMOCOUPLE

We have shown that the spin valve setup in Fig. 1(a) can, in principle, increase ZT and PF by a factor of hundreds as shown in Figs. 5 and 6. In Sec. IV A, we discuss which combination of E_0, Δ, and μ gives the largest ZT_v and PF_v. However, the parameters that give large ZT and PF do not match those of large SVEF [cf. Fig. 6(a) with Figs. 3(c) and 4(c)]. The mismatch is further elaborated in Sec. IV B.

A. *ZT* and PF with SVEF

We examine the values of ZT_v at two different Fermi energies, $\mu = -\Delta$ and Δ, shown in Figs. 7(a) and 7(b). It should be noted that optimal ZT_v is achieved at $\mu = \Delta$, despite the optimal SVEF occurring at a negative Fermi energy. The maximum value of ZT_v is approximately 0.8, which is obtained when Δ is equal to $2k_BT$ and small E_0.

In Fig. 7(c), we plot ZT_v (solid lines) and compare it with the initial ZT (dashed lines) as a function of log-scaled E_0 for $\Delta = 2k_BT$ (red lines) and $\Delta = 20k_BT$ (blue lines). The enhancement by spin valve setup, indicated by the difference between the solid and dashed line, is small at small band gap and increases a little bit as E_0 increases. On the other hand, for larger Δ, ZT_v enhances by a factor of ≈4 although the overall value of $ZT_v \approx 0.06$ is small.

Figure 7(d) shows ZT as a function of log-scaled Δ, which indicates that the optimal ZT_v is achieved when $\Delta = 2k_BT$. At the largest ZT_v value, SVEF is relatively small. The contribution relative to the change of Δ can be compared with Fig. 6(d), where the SVEF for $\mu = -\Delta$ increases as Δ increases. At lower Δ, SVEF is lower than unity, making $ZT > ZT_v$. As E_0 increases SVEF also increases but the value of ZT_v becomes smaller.

We also calculate the power factor of the spin valve configuration (PF_v). Figures 8(a) and 8(b) show the PF_v at $\mu = -\Delta$ and Δ, respectively. Similarly to ZT_v, the optimal PF_v is obtained at $\mu = \Delta$. Despite that, PF_v at $\mu = -\Delta$ is not negligible, thanks to the large SVEF for $E_0 \gg \Delta$. In Figs 8(c) and 8(d), the SVEF contribution can be seen from the distance between the solid and dashed lines. In Fig. 8(c), the same phenomenon as ZT_v also appears in PF_v, where the high PF_v (red lines) has low SVEF. From Fig. 8(d), high SVEF is found at higher E_0, which has low initial PF. On the other hand, lower E_0 has a higher initial power factor, which is shown by the red line. Figure 8(d) shows that the peak is also found at $\Delta = 2k_BT$, which indicates the optimal Δ.

Our model yields an optimal ZT_v of 0.8 and a power factor PF_v close to $7PF_0$. The decrease in power factor due to changes in parameters is not as drastic as the decrease in ZT. On the basis of these calculations, we propose a third scenario, which achieves the optimal figure of merit and power factor. When the Fermi energy is set in the lowest conduction band ($\mu = \Delta$) with low metallicity ($E_0 \approx 0.1$) and Δ around

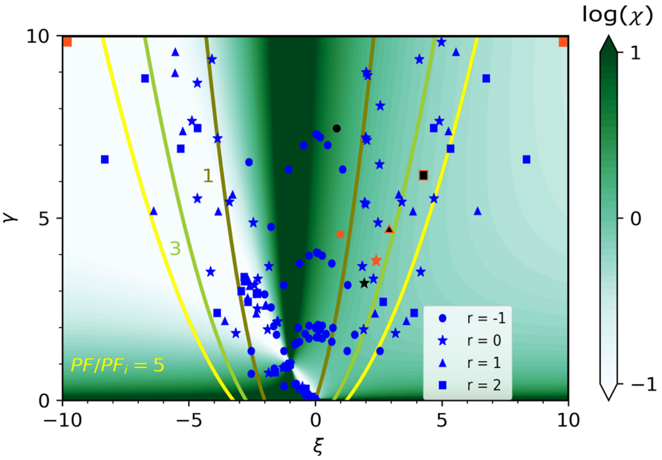

FIG. 9. 2D plot of log[χ] as a function of γ and ξ. Line plots represent the region with a certain value of PF/PF$_i$(= 1, 3, 5) and scatter markers are the data with $r = -1$, 0, 1, 2. Black markers are the maximum PF$_\mathrm{v}$ and red markers are the maximum ZT_v.

$2k_BT$ (Fig. 8), optimal PF$_\mathrm{v}$ and ZT_v are achieved. These results suggest that a suitable HMF should have a narrow band gap.

B. Mismatch of TE performance and spin valve enhancement

Figure 5 shows that the large SVEF is achieved at higher HMF metallicity (larger values of E_0); meanwhile, to get better TE performance, one needs to open the gap. At first sight, the mismatch between SVEF and TE performance might depend on the fact that we use a constant relaxation time $\tau = \tau_0(E/k_BT)^r$ with $r = 0$. We reveal the universality of our results by taking into account nonzero r. We can simplify the analysis of Eqs. (8)–(15) by writing $\sigma_m = \gamma\sigma_i$ and $\sigma_m S_m = \xi\sigma_i S_i$ with $\gamma > 0$ and ξ can be positive or negative to express $P = (1-\gamma)/(1+\gamma)$, $P' = (1-\xi)/(1+\xi)$, χ or SVEF, and

$$\mathrm{PF} = \frac{(\sigma_t S_t)^2}{\sigma_t} = \frac{(1+\gamma)^2}{(1+\xi)}\frac{(\sigma_i S_i)^2}{\sigma_i}$$

as a function of ξ and γ.

In Fig. 9, we show log(χ) as a function of ξ and γ and overlay it with lines that give PF/PF$_\mathrm{i}$ = 1 up to 6. From Fig. 9, we can see that the large SVEF is localized at large γ with small ξ or large negative ξ with $\gamma < 1$. However, the high PF/PF$_\mathrm{i}$ is found mainly in SVEF <1. We also show the spread of data points of $\Delta \in [0, 5]k_BT$ $\mu \in [-1, 1]\Delta$, $E_0 \in [0, 5]k_BT$, and $r \in [-1, 2]$. A typical half metal with large γ cannot simultaneously give large PF and SVEF. It is tempting to say that small $\gamma < 1$ and large negative ξ give both large PF and SVEF but it is not true because the lines show the relative value of PF/PF$_\mathrm{i}$ and not the absolute value. The highest values of PF$_\mathrm{v}$ and ZT_v are shown in black and red, respectively, with different marks indicating different r. We summarize the optimal γ and ξ that give the maximum ZT, PF, ZT_v, and PF$_\mathrm{v}$ in Table I.

TABLE I. Position γ and ξ of maximum TE quantities for different r.

	(γ, ξ)			
r	Maximum ZT	Maximum PF	Maximum ZT_v	Maximum PF$_\mathrm{v}$
−1	(601.4,98.7)	(1620, −473.6)	(7.5,0.75)	(4.5,0.9)
0	(275.0, −17.0)	(3.3,1.8)	(3.8,2.2)	(3.3,1.8)
1	(27.9, −18.3)	(20.8,6.8)	(4.8,3.0)	(4.8,3.0)
2	(27.9, −19.3)	(1515.4,175.7)	(6.1,4.1)	(6.1,4.1)

Maximum values of PF and ZT are located beyond the range of the plot in Fig. 9 except for max(PF) of $r = 0$ which has the same location as max (PF$_\mathrm{v}$). These maximum values of PF and ZT are located in the far right corner or the left corner of Fig. 9 with both large γ and $|\xi|$. However, in these regions, SVEF is very small and even less than 1. The optimal product of SVEF and TE performance yields PF$_\mathrm{v}$ and ZT_v with typical values of SVEF around unity. We note that with larger r values the achievable TE performance increases as shown in Appendix D (Figs. 12 and 13).

V. CONCLUSION

We found optimal parameters to achieve large ZT and PF as well as their corresponding SVEF in the HMF. The large SVEF is achieved when the degree of metallicity of the HMF is large (large E_0). On the other hand, to obtain large PF and ZT, one needs to open the band gap of HMF ($E_0 < \Delta$). The mismatch in these two optimized parameters indicates that spin valve enhancement is effective only in pure HMF without band gap, in which the TE performance is rather poor. These results are consistent with the previous finding in chromium pnictides where SVEF is large for materials with initially small ZT (CrAs, CrSb, CrBi) but small for the one that has larger ZT (CrP). The achievable ZT or ZT_v in gapless HMF cannot be as large as those with the band gap. For example, a ferromagnetic insulator (e.g. CrI$_3$) might have larger ZT than HMF but has lower SVEF. We also found that increasing the exponential factor r in the relaxation time $\tau \propto (E/k_BT)^r$ also increases the TE performance. However, this does not change the fact that the resulting optimal values of ZT_v and PF$_\mathrm{v}$ cannot be higher than the highest value of ZT and PF in gapped systems.

ACKNOWLEDGMENTS

E.H.H. acknowledges financial support from the National Research Fund Luxembourg under Grant No. C21/MS/15752388/NavSQM. A.B.C. acknowledges support from Universitas Indonesia through PUTI Grant No. NKB-368/UN2.RST/HKP.05.00/2024. I.A. acknowledges a research grant from Institut Teknologi Bandung through the Riset Peningkatan Kapasitas Dosen Muda ITB 2024 program (Grant No. STEI.PN-6-05-2024). M.S.M. acknowledges financial support from e-Asia Grant No. 4554/IT2.IV.1.2.1/T/TU.00.08/2023.

APPENDIX A: THERMOELECTRICITY OF THE 2D HALF-METAL FERROMAGNETIC INSULATOR

To analyze the thermoelectric coefficient of the half-metallic band structure illustrated in Fig. 1(b), we applied Boltzmann transport theory with

$$v^2(E) = \left(\frac{E(\mathbf{k})}{m}\right), \tag{A1}$$

$$\tau(E) = \tau_0\left(\frac{E(\mathbf{k})}{k_BT}\right)^r, \tag{A2}$$

$$\mathcal{D}(E) = \frac{m}{\pi L\hbar^2}\Theta(E), \tag{A3}$$

where $E(\mathbf{k}) = \hbar^2\mathbf{k}^2/2m$. A thermoelectric kernel using linearized Boltzmann transports gives

$$\mathcal{L}_i = \frac{\tau_0}{\pi L\hbar^2(k_BT)^r}\int E(\mathbf{k})^{r+1}(E-\mu)^i\left(-\frac{\partial f_0}{\partial E}\right)dE. \tag{A4}$$

Next, we use $\frac{\tau_0}{\pi L\hbar^2} = C$, $E/k_BT = \epsilon$, and $\mu/k_BT = \eta$ to arrive at an analytical form:

$$\mathcal{L}_i = C(k_BT)^{i+1}\int\left(\frac{E(\mathbf{k})}{k_BT}\right)^{r+1}\frac{(\epsilon-\eta)^i\exp(\epsilon-\eta)}{[\exp(\epsilon-\eta)+1]^2}d\epsilon. \tag{A5}$$

1. Insulating band kernel

Constant relaxation time approximation ($r = 0$), with dispersion energy $E_c(\mathbf{k}) = E(\mathbf{k}) - \Delta$ for the conduction band and $E_v(\mathbf{k}) = -E(\mathbf{k}) - \Delta$ for the valence band ($\widetilde{\Delta} = \Delta/k_BT$), gives

$$\mathcal{L}_{(c,v),i} = C(k_BT)^{i+1}\int\frac{(\pm\epsilon-\widetilde{\Delta})(\epsilon-\eta)^i\exp(\epsilon-\eta)}{[\exp(\epsilon-\eta)+1]^2}d\epsilon. \tag{A6}$$

Here, we introduced $\epsilon - \eta = x$, $d\epsilon = dx$, with $i = 0, 1, 2$:

$$\begin{aligned}\mathcal{L}_{(c,v),i} &= C(k_BT)^{i+1}\int\frac{x^i(\pm(x+\eta)-\widetilde{\Delta})\exp(x)}{[\exp(x)+1]^2}dx\\ &= C(k_BT)^{i+1}\left(\pm\int\frac{x^{i+1}\exp(x)}{[\exp(x)+1]^2}dx\right.\\ &\quad\left.+(\pm\eta-\bar{\Delta})\int\frac{x^i\exp(x)}{[\exp(x)+1]^2}dx\right)\end{aligned} \tag{A7}$$

for conduction band, energy range $\Delta \leqslant E < \infty$, and valence band $\Delta \leqslant -E < \infty$. So the integral boundaries $\bar{\Delta}+\eta \leqslant x < \infty$ for the conduction kernel, and $-\infty < x \leqslant -\bar{\Delta}-\eta$ for the valence band kernel:

$$\begin{aligned}\mathcal{L}_{c,i} &= C(k_BT)^{i+1}\left(\int_{\widetilde{\Delta}-\eta}^{\infty}\frac{x^{i+1}\exp(x)}{[\exp(x)+1]^2}dx\right.\\ &\quad\left.+(\eta-\bar{\Delta})\int_{\widetilde{\Delta}-\eta}^{\infty}\frac{x^i\exp(x)}{[\exp(x)+1]^2}dx\right),\end{aligned} \tag{A8}$$

$$\begin{aligned}\mathcal{L}_{v,i} &= C(k_BT)^{i+1}\left(-\int_{-\infty}^{-\widetilde{\Delta}-\eta}\frac{x^{i+1}\exp(x)}{[\exp(x)+1]^2}dx\right.\\ &\quad\left.+(-\eta-\bar{\Delta})\int_{-\infty}^{-\widetilde{\Delta}-\eta}\frac{x^i\exp(x)}{[\exp(x)+1]^2}dx\right).\end{aligned} \tag{A9}$$

Using the integrals

$$\mathcal{F}_{i,c}(\Delta) = \int_{\Delta}^{\infty}\frac{x^i\exp x}{[\exp(x)+1]^2}dx \tag{A10}$$

and

$$\mathcal{F}_{i,v}(\Delta) = -\int_{-\infty}^{-\Delta}\frac{x^i\exp x}{[\exp(x)+1]^2}dx, \tag{A11}$$

conduction and valence band kernels can be written as

$$\mathcal{L}_{c,i} = C(k_BT)^{i+1}[\mathcal{F}_{i+1,c}(\widetilde{\Delta}-\eta) - (\widetilde{\Delta}-\eta)\mathcal{F}_{i,c}(\widetilde{\Delta}-\eta)] \tag{A12}$$

and

$$\mathcal{L}_{v,i} = C(k_BT)^{i+1}[\mathcal{F}_{i+1,v}(\widetilde{\Delta}+\eta) + (\widetilde{\Delta}+\eta)\mathcal{F}_{i,v}(\widetilde{\Delta}+\eta)], \tag{A13}$$

respectively.

Integral forms on $\mathcal{F}$ can be analytically evaluated to give the following analytic forms. For the conduction band,

$$\mathcal{F}_{o,c}(x) = \frac{1}{1+e^x}, \tag{A14}$$

$$\mathcal{F}_{1,c}(x) = -\frac{xe^x}{1+e^x} + \ln(1+e^x), \tag{A15}$$

$$\mathcal{F}_{2,c}(x) = -\frac{x^2e^x}{1+e^x} + \frac{\pi^2}{3} + 2x\ln(1+e^x) + 2\mathrm{Li}_2(-e^x), \tag{A16}$$

$$\begin{aligned}\mathcal{F}_{3,c}(x) &= -\frac{x^3e^x}{1+e^x} + 3x^2\ln(1+e^x)\\ &\quad+6x\mathrm{Li}_2(-e^x) - 6\mathrm{Li}_3(-e^x).\end{aligned} \tag{A17}$$

On the other hand, the integral for the valence band obeys $\mathcal{F}_{i,v}(x) = (-1)^{i+1}\mathcal{F}_{i,c}[(-1)^i x]$, where $i = 0, 1, 2, 3$.

2. Metallic band kernel

Similar to the insulating band, the thermoelectric kernel for the metallic band has an energy range $-E_0 \leqslant E < \infty$ and

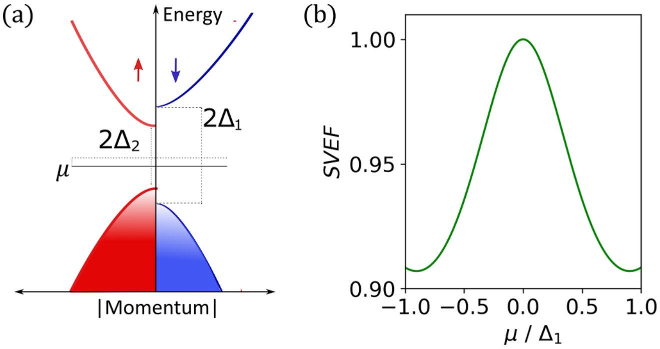

FIG. 10. (a) Band-structure illustration of the four-band model with two different band gaps. (b) SVEF of the ferromagnetic insulator by the four-band model.

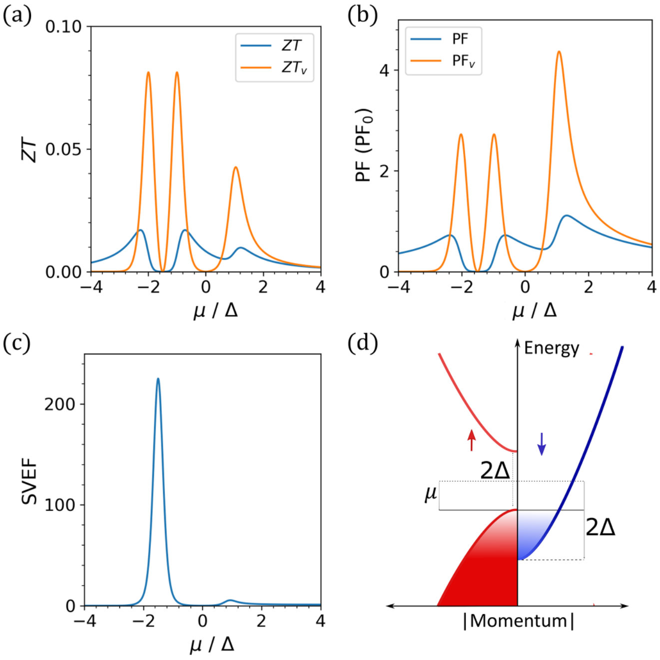

FIG. 11. (a) ZT and ZT_v and (b) PF and PF$_v$ of HMF with $E_0 = 2\Delta$ where $\Delta = 10k_BT$. (c) SVEF of the system. (d) Band-structure illustration of the system.

introduces $-\bar{E}_0 - \eta \leqslant x < \infty$ in the kernel:

$$\mathcal{L}_{m,i} = C(k_BT)^{i+1}\left(\int_{-\bar{E}_0-\eta}^{\infty}\frac{x^{i+1}\exp(x)}{[\exp(x)+1]^2}dx + (\eta+\bar{E}_0)\int_{-\bar{E}_0-\eta}^{\infty}\frac{x^{i}\exp(x)}{[\exp(x)+1]^2}dx\right) \tag{A18}$$

$$= C(k_BT)^{i+1}[\mathcal{F}_{i+1,m}(\eta+\bar{E}_0) + (\eta+\bar{E}_0)\mathcal{F}_{i,m}(\eta+\bar{E}_0)], \tag{A19}$$

where

$$\mathcal{F}_{i,m}(\bar{E}_0) = \int_{-\bar{E}_0}^{\infty}\frac{x^i\exp(x)}{[\exp(x)+1]^2}dx = \mathcal{F}_{i,c}(-E_0). \tag{A20}$$

APPENDIX B: FOUR-BAND MODEL

SVEF in ferromagnetic insulators such CrI$_3$ is modeled by using the four-band model. Each spin channel is gapped with different band gap widths [see Fig. 10(a)]. In this model, the spin-down(up) channel has a band gap width $\Delta_{1(2)}$, where $\Delta_1 > \Delta_2$:

$$\mathcal{L}_j^{(n)}(\Delta_j,\eta) = \mathcal{L}_{c,j}^{(n)}(\Delta_j,\eta) + \mathcal{L}_{v,j}^{(n)}(\Delta_j,\eta), \tag{B1}$$

where $j = 1$ or 2 representing the spin-up (down) channel and n is the exponent that gives conductivity, Seebeck coefficient, and thermal conductivity. Thermoelectric coefficients are calculated by Eqs. (5)–(7). Hence, P and P' are calculated from Eqs. (14) and (15), as

$$P = \frac{\sigma_1 - \sigma_2}{\sigma_1 + \sigma_2}, \tag{B2}$$

$$P' = \frac{\sigma_1 S_1 - \sigma_1 S_2}{\sigma_1 S_1 + \sigma_2 S_2}. \tag{B3}$$

The SVEF of the ferromagnetic insulator is calculated by Eqs. (13) by the four-band model plotted in Fig. 10(b).

APPENDIX C: THERMOELECTRICITY FOR $\mu < -\Delta$

In the main text, we limit the value of μ between $[-\Delta, \Delta]$. It is possible for HMF to have μ lower than $-\Delta$ as long as $E_0 > \Delta$ as shown in Fig. 11(d). In Figs. 11(a)–11(c), we show that for the case of HMF with $E_0 = 2\Delta$, the thermoelectric quantities (ZT, PF, and SVEF) at $\mu = -\Delta$ are equal to those at $\mu = -2\Delta$. In general, for $E_0 = c\Delta$, the thermoelectric quantities at $\mu = -\Delta$ are equal to those at $\mu = -c\Delta$.

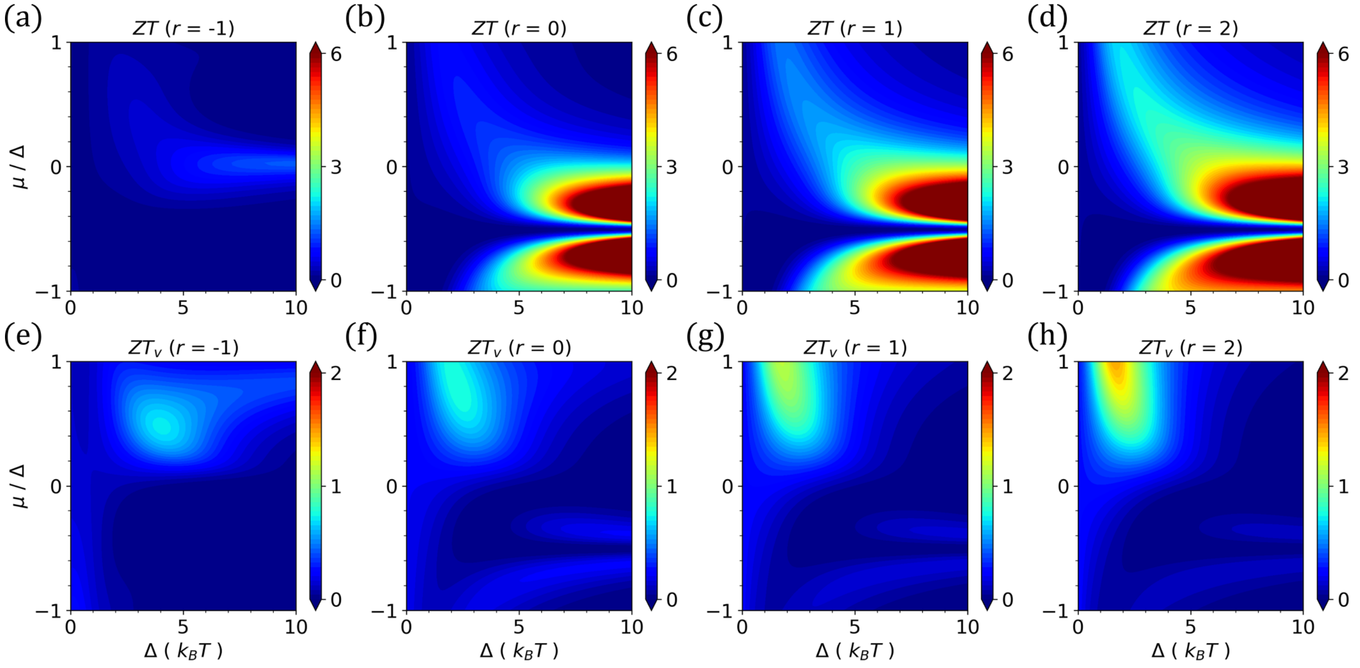

FIG. 12. (a)–(d), (e)–(h) ZT and ZT_v, respectively, for various r from -1 to 2 as a function of Fermi energy μ and Δ for $E_0 = 0.1k_BT$.

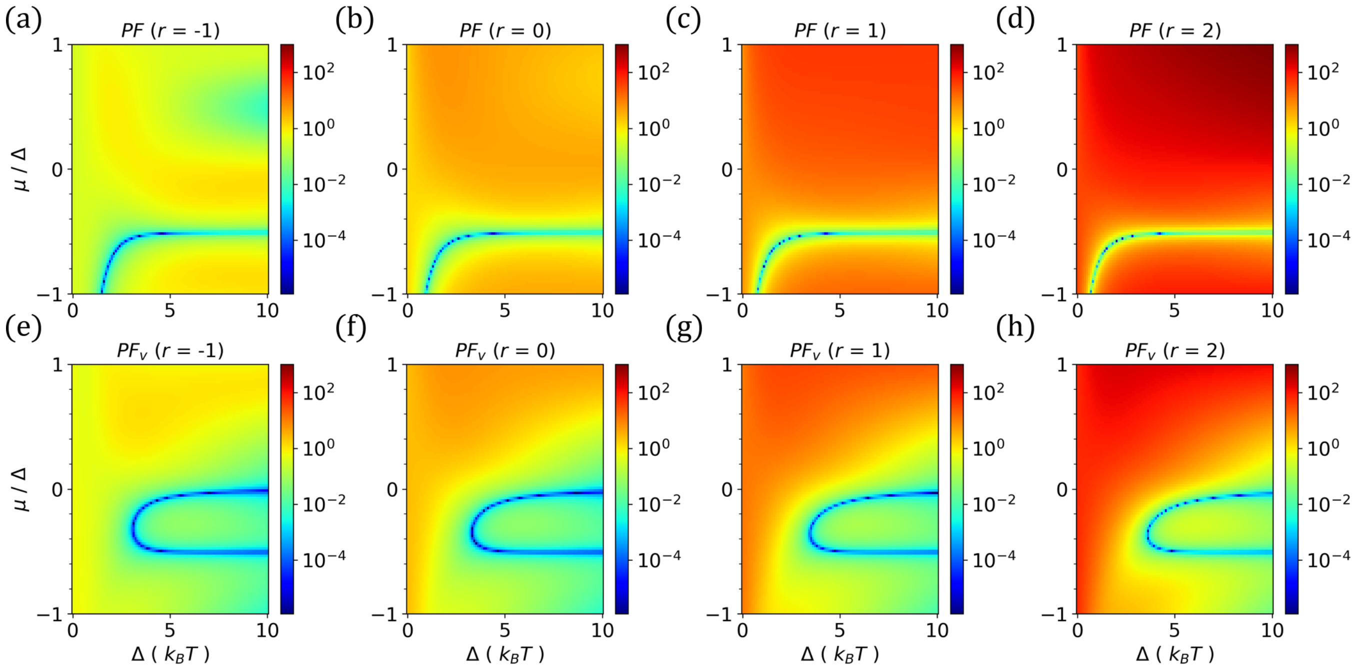

FIG. 13. (a–d, e–h) PF and PF$_v$, respectively, for various r from -1 to 2 as a function of Fermi energy μ and Δ for $E_0 = 0.1k_BT$.

APPENDIX D: ENERGY-DEPENDENT RELAXATION TIME

Dependence of relaxation time on energy is calculated using Eqs. (A2). We calculate figure of merit and power factor for different r as shown in Figs. 12 and 13. Thermoelectric kernels for each relaxation time are calculated using Eqs. (A5). The results show that relaxation time changes influence the ZT enhancement by SVEF. When relaxation time is inverse proportional to energy, SVEF can improve the ZT of HMF. This is the same as shown in Fig. 9, where the circle markers tend to be located at regions with high SVEF. The power factor in Fig. 13 shows that r change improves the power factor of HMF the same as with the ZT, and at the same time SVEF is decreased.

---

[1] N. T. Hung, E. H. Hasdeo, A. R. T. Nugraha, M. S. Dresselhaus, and R. Saito, Quantum effects in the thermoelectric power factor of low-dimensional semiconductors, Phys. Rev. Lett. **117**, 036602 (2016).

[2] L. D. Hicks and M. S. Dresselhaus, Thermoelectric figure of merit of a one-dimensional conductor, Phys. Rev. B **47**, 16631 (1993).

[3] L. D. Hicks and M. S. Dresselhaus, Effect of quantum-well structures on the thermoelectric figure of merit, Phys. Rev. B **47**, 12727 (1993).

[4] J. P. Heremans, M. S. Dresselhaus, L. E. Bell, and D. T. Morelli, When thermoelectrics reached the nanoscale, Nat. Nanotechnol. **8**, 471 (2013).

[5] Y. Pei, H. Wang, and G. J. Snyder, Band engineering of thermoelectric materials, Adv. Mater. **24**, 6125 (2012).

[6] R. Wang, S. Luo, X. Mo, H. Liu, T. Liu, X. Lei, Q. Zhang, J. Zhang, and L. Huang, Optimization of thermoelectric property of n-type Mg_3Sb_2 near room temperature via Mn&Se co-doping, Adv. Sustainable Syst. **7**, 2300234 (2023).

[7] S.-Z. Huang, C.-G. Fang, Q.-Y. Feng, B.-Y. Wang, H.-D. Yang, B. Li, X. Xiang, X.-T. Zu, and H.-X. Deng, Strain tunable thermoelectric material: Janus ZrSSe monolayer, Langmuir **39**, 2719 (2023).

[8] C.-W. Wu, X. Ren, G. Xie, W.-X. Zhou, G. Zhang, and K.-Q. Chen, Enhanced high-temperature thermoelectric performance by strain engineering in bioCl, Phys. Rev. Appl. **18**, 014053 (2022).

[9] M. Gaffar, S. A. Wella, and E. H. Hasdeo, Effects of topological band structure on thermoelectric transport of bismuthene, Phys. Rev. B **104**, 205105 (2021).

[10] N. Xu, Y. Xu, and J. Zhu, Topological insulators for thermoelectrics, npj Quantum Mater. **2**, 471 (2013).

[11] G. K. Goyal, S. Mukherjee, R. C. Mallik, S. Vitta, I. Samajdar, and T. Dasgupta, High thermoelectric performance in $Mg_2(Si_{0.3}Sn_{0.7})$ by enhanced phonon scattering, ACS Appl. Energy Mater. **2**, 2129 (2019).

[12] W. Kim, Strategies for engineering phonon transport in thermoelectrics, J. Mater. Chem. C **3**, 10336 (2015).

[13] S. Xie, H. Zhu, X. Zhang, and H. Wang, A brief review on the recent development of phonon engineering and manipulation at nanoscales, Int. J. Extreme Manuf. **6**, 012007 (2024).

[14] R. Franz and G. Wiedemann, Ueber die wärmeleitungsfähigkeit der metalle, Ann. Phys. (Leipzig) **165**, 497 (1853).

[15] J. Mao, H. Zhu, Z. Ding, Z. Liu, G. A. Gamage, G. Chen, and Z. Ren, High thermoelectric cooling performance of n-type Mg_3Bi_2-based materials, Science **365**, 495 (2019).

[16] G. Yang, L. Sang, C. Zhang, N. Ye, A. Hamilton, M. S. Fuhrer, and X. Wang, The role of spin in thermoelectricity, Nat. Rev. Phys. **5**, 466 (2023).

[17] A. B. Cahaya, O. A. Tretiakov, and G. E. W. Bauer, Spin Seebeck power conversion, IEEE Trans. Magn. **51**, 1 (2015).

[18] M. Hatami, G. E. W. Bauer, Q. Zhang, and P. J. Kelly, Thermoelectric effects in magnetic nanostructures, Phys. Rev. B **79**, 174426 (2009).

[19] M. S. Muntini, E. Suprayoga, S. A. Wella, I. Fatimah, L. Yuwana, T. Seetawan, A. B. Cahaya, A. R. T. Nugraha, and E. H. Hasdeo, Spin-tunable thermoelectric performance in monolayer chromium pnictides, Phys. Rev. Mater. **6**, 064010 (2022).

[20] W. Choi, H. Nishiyama, Y. Ogawa, Y. Ueno, K. Furukawa, T. Takeuchi, Y. Tsutsui, T. Sakurai, and S. Seki, Relaxation of plasma carriers in graphene: An approach by frequency-dependent optical conductivity measurement, Adv. Opt. Mater. **6**, 1701402 (2018).

[21] A. Patel, D. Singh, Y. Sonvane, P. B. Thakor, and R. Ahuja, High thermoelectric performance in two-dimensional Janus monolayer material Ws-X (X = Se and Te), ACS Appl. Mater. Interfaces **12**, 46212 (2020).

[22] V. V. Kruglyak, R. J. Hicken, M. Ali, B. J. Hickey, A. T. G. Pym, and B. K. Tanner, Measurement of hot electron momentum relaxation times in metals by femtosecond ellipsometry, Phys. Rev. B **71**, 233104 (2005).

[23] H. Sheng, Y. Zhu, D. Bai, X. Wu, and J. Wang, Thermoelectric properties of two-dimensional magnet CrI_3, Nanotechnology **31**, 315713 (2020).